Thai Environmental Engineering Journal Vol. 38 No. 2 (2024) : 79-90
www.eeat.or.th

Adsorption Mechanisms of Haloacetonitriles on Adsorbent Derived from Canvas Fabric

Kanlayanee Yimyam[1,2,3], Aunnop Wongrueng[3] and Pharkphum Rakruam[3*]

[1]Graduate School, Chiang Mai University, Chiang Mai 50200, Thailand
[2]Doctor of Engineering Program in Environmental Engineering, Faculty of Engineering, Chiang Mai University, Chiang Mai 50200, Thailand
[3]Department of Environmental Engineering, Faculty of Engineering, Chiang Mai University, Chiang Mai 50200, Thailand
[*]E-mail : pharkphum@eng.cmu.ac.th

Article History; *Received: 23 August 2024, Accepted: 26 August 2024, Published: 30 August 2024*

Abstract

The adsorption mechanisms of HANs on canvas fabric-derived adsorbent and modified adsorbent with ferric chloride and ferric nitrate solution were investigated. With the ferric nitrate modification (CF-Fe$(NO_3)_3$), the pore structure of the adsorbent was mesopore, while other adsorbents were micropore. With the mesopore structure of CF-Fe$(NO_3)_3$, the adsorption occurred both on the outer pore layer and inside the pore surface, which resulted in the highest adsorption efficiency obtained by the CF-Fe$(NO_3)_3$ adsorbent. Furthermore, the adsorption mechanisms of five HAN species were investigated. Physical adsorption is the main mechanism of HANs on CF-Fe$(NO_3)_3$ adsorbent based on the low adsorption energy determined from the D-R isotherm. The fastest HAN species to reach equilibrium and the highest removal by the CF-Fe$(NO_3)_3$ adsorbent was TCAN, which has the lowest solubility and more hydrophobicity. Besides the low solubility of HANs species, the halogen atom of each HANs species also affected the removal efficiency. HANs species with more halogen atoms showed higher removal efficiency than other HANs species with low halogen atoms.

Keywords : adsorption kinetics; adsorption isotherm; chemical activation; haloacetonitriles; low-cost adsorbent

Introduction

Critical to the process of treating drinking water is disinfection. Its objective is to assist in the destruction of waterborne pathogens. The chlorine chemicals used to disinfect water sources not only stop the growth of various pathogens, but they can also react with organic and inorganic compounds to create disinfection by-products (DBPs) [1]. Currently, research shows that aromatic DBPs [2] and nitrogen-containing DBPs (N-DBPs) [3] are more harmful than controlled DBPs. Haloacetonitriles (HANs) are a category of N-DBPs that are detected in disinfected drinking water [4]. Dichloroacetonitrile (DCAN) was the most commonly found HANs compound among the 9 HANs species, followed by bromochloroacetonitrile (BCAN) and dibromoacetonitrile (DBAN) [5, 6]. Its carcinogenic and mutagenic characteristics render it a significant threat to human health [7, 8].

There are various available techniques applied for the removal of HANs, including boiling [9, 10], photocatalytic degradation [11], degradation with the UV/peroxymonosulfate process [12], catalytic hydrolysis [13], and adsorption [14]. The adsorption technique is one of the most prominent methods for removing

HANs from contaminated water. Previous research has examined the absorption of haloacetonitriles using polymerizable surfactant-modified mesoporous silica. The incorporation of a polymerizable surfactant was discovered to enhance the efficacy of HANs adsorption. Furthermore, as the degree of halogen substitution in the HANs molecule increased, so did its hydrophobicity. This had an effect on the organic partition's ability to adsorb things [15]. Later in 2019, Prarat et al. investigated the mechanisms and effects of porous structures on the adsorption of haloacetonitriles on silica-based materials. The researchers discovered that the crystalline and porous structures of the materials, specifically the size and volume of the pores as well as the surface functional group of the adsorbent, had a significant impact on the adsorption of HANs.

Besides the sorbents that have been previously mentioned, activated carbon is an additional intriguing sorbent. Activated carbons are efficient adsorbents widely utilized in various applications, including medical purposes, gas storage, pollutant and odor elimination, gas purification and separation, and catalysis [16]. Numerous varieties of DBPs were adsorbed on activated carbon. Qian et al. [17] investigated the adsorption of haloforms by five various granular activated carbons (GACs). The Freundlich model performed well in describing adsorption isotherms, while the pseudo-second-order model performed well in describing adsorption kinetics. The rate-limiting process was identified as film diffusion, while haloforms were adsorbed through chemical adsorption. In general, there was no relationship between the quantity of haloform adsorption and the surface area of GAC. According to research by Nakamura et al. [18], the amount of absorbed trihalomethane is related to the level of hydrophobicity of the activated carbon fiber surface. The degree of adsorption for trihalomethane containing bromine was greater than that containing chlorine. The polarity of trihalomethane molecules can explain the variations in the amounts adsorbed among trihalomethanes.

Currently, the production of activated carbon uses low-cost materials like durian shells [19], bamboo, coconut shells [20], and fabric [21]. Fabric is an interesting substance that can be used as an adsorbent because its primary component is carbon [22]. Furthermore, there has been a significant increase in the amount of textile waste [23]. Consequently, this issue poses a challenge, necessitating the exploration of recycling or utilization methods to address these concerns.

For an understanding of the adsorption mechanism, this study focused on investigating the relationship between the porous structures of the adsorbent derived from canvas fabric and the adsorption efficiency of DBAN at low concentrations. The data from the experiments were matched with adsorption isotherm models, and the kinetic parameters were figured out to find the most likely adsorption mechanism(s). In addition, the effect of the five species of HANs including BCAN, DBAN, DCAN, monobromoacetonitrile (MBAN), and trichloroacetonitrile (TCAN) on the adsorption mechanism was also investigated.

Methodology

Adsorbent Synthesis

This study synthesized the canvas fabric-derived adsorbent. The methodology for synthesizing canvas fabric derived adsorbent was reported in a previous study [24]. Two ferric chemical solutions were used to activate the adsorbent including ferric chloride ($FeCl_3$) and ferric nitrate ($Fe(NO_3)_3$). The methodology for adsorbent activation was also reported in a previous study [24]. This study used three different adsorbents: canvas fabric-derived adsorbent (CF), activated canvas fabric-derived adsorbent with ferric chloride (CF-$FeCl_3$), and activated canvas fabric-derived adsorbent with ferric nitrate (CF-$Fe(NO_3)_3$). The BET surface areas of CF, CF-$FeCl_3$, and CF-$Fe(NO_3)_3$ are 262.51, 577.25, and 370.83 m^2/g, respectively.

Adsorption Kinetics Experiments

The adsorption kinetics experiments were divided into two experiments. The first experiment examined DBAN adsorption kinetics using CF, CF-$FeCl_3$, and CF-$Fe(NO_3)_3$ adsorbents. In this experiment, DBAN was used to represent HANs. DBAN was prepared as a stock solution by mixing in a 10 mM phosphate buffer at pH 7. The adsorption kinetics were

conducted by using each adsorbent at 0.1 g with an initial DBAN concentration of 50 µg/L. The volume of each sample was fixed at 100 mL. The experiment was performed under shaking at 200 rpm at room temperature by varying the contact time from 0 to 300 minutes. The pH was controlled at 7. The water samples were filtrated through a 0.22 µm nylon unit filter and measured for the remaining DBAN concentration. The residual DBAN concentration in the liquid solution was determined by using a gas chromatograph combined with an electron capture detector (GC/ECD) (Hewlett Packard, HP6890 GC, USA). The procedure adhered to EPA Method 551.1, as specified by the US Environmental Protection Agency [6].

The second experiment was conducted with CF-Fe$(NO_3)_3$ adsorbent. Five HANs species were prepared as stock solutions by mixing in a 10 mM phosphate buffer with a controlled pH of 7. The amount of 0.1 g of CF-Fe$(NO_3)_3$ adsorbent was used in this experiment with the same conditions as the adsorption kinetics of DBAN. The residual HANs species in the liquid was detected by using a gas chromatograph combined with an electron capture detector (GC/ECD) (Hewlett Packard, HP6890 GC, USA). The procedure adhered to EPA Method 551.1, as specified by the US Environmental Protection Agency [6].

The adsorption rate was investigated by fitting the model, which included a linear driving force model, a pseudo-second-order kinetic model, and an intraparticle diffusion model.

The equation for the pseudo-second-order model was illustrated in Eq. (1) [25], where q_t is the adsorption capacity at time (mg/g) and q_e is the adsorption capacity at equilibrium (mg/g), k_2 is the pseudo-second-order rate constant (g/mg.min), and t is the adsorption time (min), respectively.

$$q_t = \frac{k_2 q_e^2 t}{1+k_2 q_e t} \quad (1)$$

To measure the adsorption rate, the initial adsorption rate, h (µg/g.hr) at t = 0, and the half-life time, $t_{1/2}$ (hr), can be determined according to Eq. (2) and (3), respectively.

$$h = k_2 q_e^2 \quad (2)$$

$$t_{1/2} = \frac{1}{k_2 q_e} \quad (3)$$

The equation for the linear driving force model is illustrated in Eq. (4), where K_p (L/g) is the linear solid/liquid adsorption distribution coefficient, and k_{LDF} is the linear driving force coefficient at time (t) (µg/g). The q_s is the adsorption capacity at the particle surface (µg/g), and X is the adsorbent dose (g/L).

$$q_t = q_e(1\text{-}e^{-(1+K_p X)K_{LDF} t}) \quad (4)$$

The intraparticle diffusion model proposed by Weber and Morris [26] was utilized to determine the adsorption process in cases where the adsorption process was limited by mass transfer or diffusion. The equation for the intraparticle diffusion model can be defined as shown in Eq. (5), where k_p is the intraparticle diffusion rate constant (µg/g/min0.5) and C (µg/g) is the Y-intercept constant that relates to the thickness of the boundary layer. In addition, the intraparticle diffusion coefficient D_p (m^2/s) in the adsorbent particle with a homogeneous structure is simply calculated from Eq. (6) [27].

$$q_t = k_p t^{0.5} + C \quad (5)$$

$$D_p = \frac{R^2 k_{LDF}}{15} \quad (6)$$

The adsorption kinetic models were applied to the experimental data and the relative root mean square error (RRSME) was calculated by nonlinear regression using Microsoft Excel 2011 software.

Adsorption Isotherm Experiments

The adsorption isotherm experiments were divided into two experiments, the same as the adsorption kinetics experiments. The first experiment was conducted with an initial concentration of DBAN ranging from 25 to 150 µg/L under the same conditions as the kinetics experiment, except the contact time that was fixed at 60 minutes. The second experiment was conducted with five species of HANs with concentrations in the range of 25 to 150 µg/L. The adsorption isotherm was investigated by fitting to the models, namely the linear,

Freundlich, Redlich-Peterson (R-P), and Dubinin-Radushkevich (D-R) isotherm models.

The linear model is the simplest isotherm model that can be used to describe the relationship between adsorption capacity and equilibrium concentration, especially at low concentrations. The linear isotherm is described by Eq. (7), where C_e is the equilibrium concentration of DBAN and K_P is the linear partition coefficient obtained from the slope of the relationship between q_e (µg/g) and C_e (µg/L).

$$q_e = K_P C_e \quad (7)$$

The Freundlich isotherm model is an empirical equation used to describe the heterogeneous system as shown in Eq. (8), where K_F (µg/g) and n are Freundlich constants.

$$q_e = K_F C_e^{1/n} \quad (8)$$

The Redlich-Peterson (R-P) isotherm model is a combination of the Langmuir and Freundlich isotherm, which can describe adsorption mechanisms in a mixed system and does not follow the ideal monolayer adsorption. The equation is shown as Eq. (9), where K_R (L/g) is the Redlich-Peterson constant, B (L/µg) is the Redlich-Peterson constant value, and β_R is an exponent that ranges from 0 to 1.

$$q_e = \frac{K_R C_e}{1+BC_e^{\beta_R}} \quad (9)$$

The Dubinin-Radushkevich (D-R) isotherm is one of the empirical models utilized to describe the adsorption mechanisms that are associated with Gaussian energy distribution on the heterogeneous surface. The D-R isotherms equation is shown as Eq. (10) to (12), where ε is the Polanyi potential, β is the Dubinin-Radushkevich constant value (mol^2/J^2), R is the universal gas constant (8.314×10^{-3} KJ mol^{-1} K^{-1}), T is the absolute temperature (°K), q_{DR} is the theoretical isotherm saturation capacity (µg/g), and E is the mean free adsorption energy (J/mol).

$$q_e = q_{DR} exp^{-(\beta\varepsilon^2)} \quad (10)$$

$$\varepsilon = RT\, ln\left(1+\frac{1}{C_e}\right) \quad (11)$$

$$E = \frac{1}{\sqrt{2\beta}} \quad (12)$$

The adsorption isotherm models were applied to the experimental data and the relative root mean square error (RRSME) was calculated by nonlinear regression using Microsoft Excel 2011 software.

Results and Discussions

Adsorption Kinetic

Adsorption kinetic of DBAN removal using CF, CF-$FeCl_3$, and CF-$Fe(NO_3)_3$ adsorbent.

The kinetic curves of DBAN adsorption by three adsorbents are shown in Fig. 1. These curves show the relative adsorption capacity changes over time. According to the results, the adsorption rate of all adsorbents showed a high degree of velocity at an initial stage and then significant deceleration before reaching equilibrium. Based on the kinetic curves shown in Figure 1, DBAN adsorption with all adsorbents reached equilibrium within 60 minutes. However, the adsorbed concentration of DBAN on each adsorbent was varied. CF-$Fe(NO_3)_3$ adsorbent shows the highest adsorbed concentration, followed by CF-$FeCl_3$ and CF, respectively.

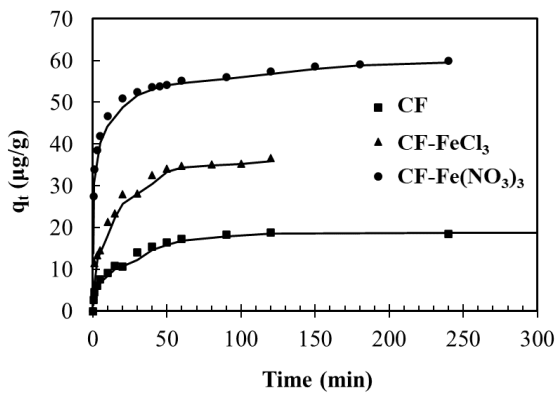

Figure 1 Adsorption kinetic of DBAN on CF, CF-$FeCl_3$, and CF-$Fe(NO_3)_3$

Various mathematical expression models were utilized to characterize the adsorption processes. From the obtained results, it was found that the concentration of adsorbate in the solution is the driving force, and the area represents the number of active sites on the

adsorbent surface. So, the pseudo-second-order model is a better way to describe the mechanism of DBAN sticking to the porous adsorbents when the concentration of the solute is low. Wu et al. [28] revealed that the pseudo-second-order model was suitable to explain the adsorption of low molecular weight compounds on small adsorbent particles. In this case, the adsorption rate is based on the adsorption capacity, not the concentration of the adsorbate. Table 1 shows the adsorption kinetic parameters of CF, CF-$FeCl_3$, and CF-$Fe(NO_3)_3$, which were calculated from the linear driving force and pseudo-second-order models. The D_p value is used to describe the mechanism of adsorption on the outer pore layer of the adsorbent. The high value of D_p indicated that the adsorption occurs in the outer pore layer. The obtained D_p values of DBAN adsorbed onto CF-$Fe(NO_3)_3$, which performed extremely high adsorption capacities, were lower than those of CF and CF-$FeCl_3$. It can be indicated that the adsorption by CF-$Fe(NO_3)_3$ was not only absorbed on the outer pore layer alone but also adsorbed inside the pore surface. While the adsorption by CF and CF-$FeCl_3$ occurs quickly and mainly occupies on the outer pore layer of the adsorbent due to its small porosity. These results corresponded with the porosity of CF, CF-$FeCl_3$, and CF-$Fe(NO_3)_3$ which reported that the porosity of CF and CF-$FeCl_3$ was micropore (<2 nm) while CF-$Fe(NO_3)_3$ was mesopore (2-15 nm) [24].

The initial adsorption rate and half-life time of DBAN by CF-$Fe(NO_3)_3$ were faster than those of CF and CF-$FeCl_3$ due to the larger pore volume of CF-$Fe(NO_3)_3$, which was 1.9 and 1.2 times greater than those of CF and CF-$FeCl_3$, respectively. Moreover, the pore size of CF-$Fe(NO_3)_3$ was 1.3 and 1.8 times larger than that of CF and CF-$FeCl_3$, respectively. This is consistent with previous studies that reported that the adsorption rate of the porous material is related to the porous structure of the sorbent [14, 29]. Therefore, the different adsorption behaviors of CF, CF-$FeCl_3$, and CF-$Fe(NO_3)_3$ may be due to the nature specificity of the structure with direct porous.

Furthermore, adsorption kinetics might be related to intra-pore diffusion. In general, the adsorption process in the aqueous phaseinvolves three successive mass transfer steps including the film or external diffusion, the intraparticle or pore diffusion, and adsorption at the active site of the adsorbent's surface [30]. However, the last step is usually left out of kinetic analyses because it happens quickly. Thus, the rate-limiting step might be determined between film diffusion and intraparticle diffusion.

Hence, the intra-pore diffusion equation was utilized to predict adsorption kinetics. The results qt versus $t_{1/2}$ for DBAN adsorption with CF, CF-$FeCl_3$, and CF-$Fe(NO_3)_3$ are shown in Figure 2. The results showed that various adsorption phases

were involved in the adsorption process. In Figure 2, the influence of boundary diffusion was detected on the first slope, while the influence of pore diffusion was detected on the second slope. According to the intraparticle diffusion model, if intraparticle diffusion is involved in adsorption, the relationship between q_t and $t_{1/2}$ should be linear. Thus, it can be confirmed that intraparticle diffusion was involved in the adsorption process for all adsorbents.

The relationship between q_t and $t_{1/2}$ can be used to indicate the rate-limiting step of intraparticle diffusion. If the linear line passes through the origin, intraparticle diffusion is the rate-limiting step. Whereas if the linear line does not pass through the origin, this indicates that intraparticle diffraction is not the sole rate-limiting step. Other kinetic models also regulate the rate of adsorption [31]. From Figure 2, the linear line between q_t and $t_{1/2}$ does not pass through the origin. Thus, it can be indicated that intraparticle diffraction is not the sole rate-limiting step of the adsorption process for all adsorbents.

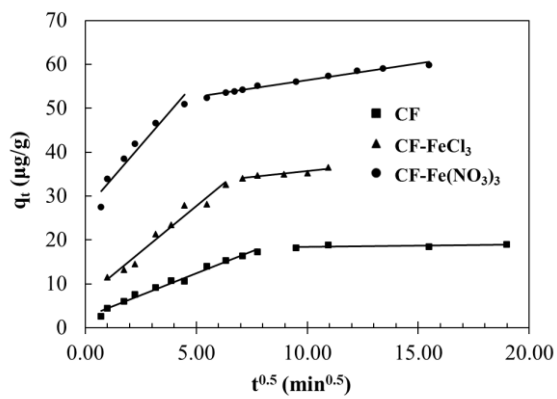

Figure 2 The intraparticle diffusion model of DBAN on CF, CF-$FeCl_3$, and CF-$Fe(NO_3)_3$

Table 1 Kinetic parameters of DCAN adsorption onto CF, CF-$FeCl_3$, and CF-$Fe(NO_3)_3$ using linear driving force and pseudo-second-order model

Materials	$q_{e\ exp}$ (µg/g)	linear driving force model				
		$q_{e\ cal}$ (µg/g)	k_{LDF} (1/s)	k_L (cm/s)	D_p (cm^2/s)	RRSME (µg/g)
CF	17.3	18.8	33.0×10^{-5}	24.7×10^{-5}	55.0×10^{-11}	2.01
CF-$FeCl_3$	34.0	35.8	29.1×10^{-5}	16.1×10^{-5}	48.5×10^{-11}	1.37
CF-$Fe(NO_3)_3$	55.1	58.3	8.40×10^{-5}	2.35×10^{-5}	2.24×10^{-11}	1.27
Materials	$q_{e\ exp}$ (µg/g)	**pseudo-second-order model**				
		$q_{e\ cal}$ (µg/g)	k_2 (g/µg·min)	h (µg/g·min)	$t_{1/2}$ (min)	RRSME (µg/g)
CF	17.3	19.5	0.005	2.0	9.9	<0.2
CF-$FeCl_3$	34.0	37.7	0.004	5.5	6.9	1.75
CF-$Fe(NO_3)_3$	55.1	55.3	0.023	72.0	0.8	3.19

Table 2 Parameters of the intraparticle diffusion model of DBAN adsorbed on CF, CF-$FeCl_3$, and CF-$Fe(NO_3)_3$

Materials	k_{p1} (µg/g /$min^{0.5}$)	C_1 (µg/g)	R_1^2	k_{p2} (µg/g /$min^{0.5}$)	C_2 (µg/g)	R_2^2
CF	2.00	2.43	0.984	0.05	17.98	0.363
CF-$FeCl_3$	4.16	6.89	0.968	0.55	30.23	0.874
CF-$Fe(NO_3)_3$	5.83	26.99	0.930	0.76	48.85	0.981

The estimated parameters of the intraparticle diffusion model are shown in Table 2 which illustrates that the rate constant (k_p) of CF-$Fe(NO_3)_3$ was higher than those of CF and CF-$FeCl_3$. This indicated that the rate of DBAN solution moving through a CF-$Fe(NO_3)_3$ adsorbent was faster than that of CF and CF-$FeCl_3$ adsorbents both through film or external diffusion and intraparticle diffusion. This is well consistent with the study of Panida et al. [14], which reported that the adsorption rate was affected by the pore size of the sorbent, with the intraparticle diffusion rate constants of mesoporous materials were higher than those of microporous materials. In addition, it was found that the slopes of the second linear (k_{p2}) of DBAN adsorbed on CF, CF-$FeCl_3$, and CF-$Fe(NO_3)_3$ were less than the slopes of the first linear (k_{p1}). It can be concluded that intraparticle diffusion should restrict the adsorption rate.

Adsorption kinetic of five HANs species removal using CF-Fe(NO$_3$)$_3$ adsorbent.

Based on the results in Figure 1 and 2, the CF-$Fe(NO_3)_3$ adsorbent was found to provide high efficiency to remove DBAN species. Then, the CF-$Fe(NO_3)_3$ adsorbent was selected and used to investigate the removal efficiency for five HANs species. The results of the adsorption kinetics of five HANs species are shown as the kinetics curve in Figure 3.

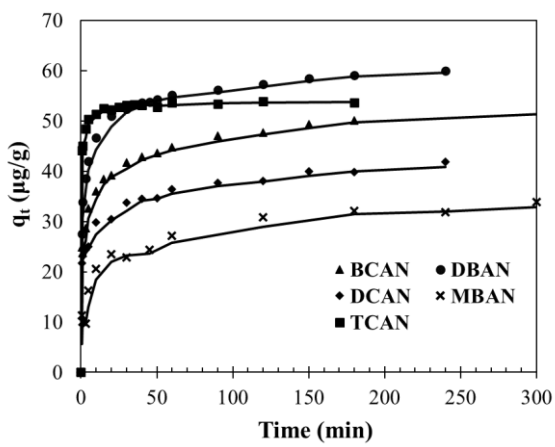

Figure 3 Adsorption kinetic of five HANs on CF-$Fe(NO_3)_3$

The results indicated that the initial rate of adsorption was fast and was significant deceleration before reaching equilibrium. TCAN species exhibit the fastest rate of approaching equilibrium within 30 minutes. The other species, including MBAN, DBAN, BCAN, and DCAN, required 180 minutes to reach equilibrium. The molecular surface characteristics of

various HANs might be impacting the rate of reaching equilibrium. HANs species that had low solubility reached equilibrium faster. The solubility of each HANs species was affecting the rate of reaching equilibrium. The solubility of each species from high to low was MBAN, DBAN, DCAN, and TCAN, respectively [14]. Thus, TCAN, with the lowest solubility, was the fastest to reach equilibrium, followed by the other species. The low solubility of HANs species can be used to indicate the hydrophobicity of the solution. HANs species with low solubility have more hydrophobicity and tend to adsorb on the adsorbent. Thus, the hydrophobicity of the solution also affected the time for reaching equilibrium.

Table 3 shows the kinetic parameters of five HANs adsorption onto CF-Fe$(NO_3)_3$ calculated from the linear driving force and the pseudo-second-order model. The adsorption kinetics model was investigated using the RRSME value. The RRSME is the differential value between the obtained value from the experiment and the calculated value from the equation. The adsorption kinetics model with a lower RRSME value indicated the adsorption kinetics was matched with this model. When comparing the RRSME of the linear driving force and the pseudo-second-order model. It was found that the adsorption kinetics of five HANs onto adsorbents were well matched to the linear driving force model with a lower RRSME value than the pseudo-second-order model.

Among the HANs species, TCAN was mostly adsorbed on CF-Fe$(NO_3)_3$ with the highest K_{LDF} value due to the lowest solubility of TCAN which indicated TCAN was more hydrophobic than other species. The D_p value of five HANs on CF-Fe$(NO_3)_3$ is in the order of TCAN > MBAN > DCAN > BCAN > DBAN, respectively which well corresponds with the adsorption capacities of each HANs species.

Adsorption isotherms

Adsorption kinetic of five HANs species removal using CF-Fe$(NO_3)_3$ adsorbent.

In this study, four distinct adsorption isotherm models, i.e., Linear isotherm, Freundlich isotherm model, Dubinin–Radushkevich isotherm model, and Redlich–Peterson isotherm model, were used to describe the adsorption mechanism of DBAN and synthesized adsorbents. Four isotherm models were applied in this study because all isotherm models were compatible with the low range of equilibrium concentration used in this study (0–125 μg/L).

As shown in Figure 4, the isotherm data shows only a linear function due to the low concentration of DBAN used in this study. So, these phenomena are not appropriate for forecasting the maximal HAN adsorption capacity with a nonlinear isotherm model. From the results, CF-Fe$(NO_3)_3$ shows the highest adsorption capacity of DBAN, followed by CF-$FeCl_3$ and CF, respectively.

Table 3 Kinetic parameters of five HANs adsorption onto CF-Fe$(NO_3)_3$ using linear driving force and pseudo-second-order model

Materials	$q_{e\,exp}$ (μg/g)	linear driving force model				
		$q_{e\,cal}$ (μg/g)	k_{LDF} (1/s)	k_L (cm/s)	D_p (cm^2/s)	RRSME (μg/g)
BCAN	44.7	49.7	14.0×10^{-5}	3.92×10^{-5}	3.73×10^{-11}	2.01
DBAN	55.1	58.3	8.40×10^{-5}	2.35×10^{-5}	2.24×10^{-11}	1.37
DCAN	31.9	35.5	21.0×10^{-5}	5.88×10^{-5}	5.60×10^{-11}	1.27
MBAN	30.8	33.4	21.5×10^{-5}	6.03×10^{-5}	5.74×10^{-11}	1.52
TCAN	53.1	53.4	24.0×10^{-5}	6.71×10^{-5}	6.39×10^{-11}	0.36
Materials	$q_{e\,exp}$ (μg/g)	**pseudo-second-order model**				
		$q_{e\,cal}$ (μg/g)	k_2 (g/μg·min)	h (μg/g·min)	$t_{1/2}$ (min)	RRSME (μg/g)
BCAN	44.7	45.5	0.021	43.5	1.0	4.37
DBAN	55.1	55.3	0.023	72.0	0.8	3.19
DCAN	31.9	32.0	0.030	31.2	1.0	3.45
MBAN	30.8	32.2	0.005	5.7	5.7	3.08
TCAN	53.1	52.9	0.150	419	0.1	<0.2

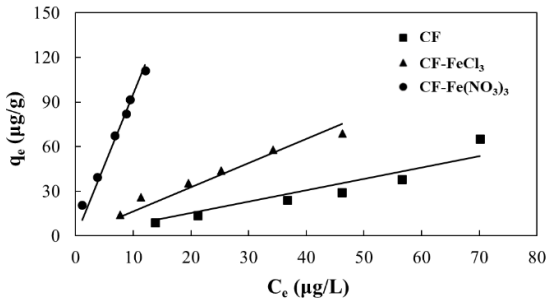

Figure 4 Adsorption isotherm of DBAN on CF, CF-$FeCl_3$, and CF-$Fe(NO_3)_3$

Isotherm parameters for DBAN adsorption on CF, CF-$FeCl_3$, and CF-$Fe(NO_3)_3$ are shown in Table 4. The correlation coefficient (RRSME) of DBAN adsorption on all adsorbents was fitted with the linear and Redlich-Peterson isotherm models, with the range of RRSME at 4.41-6.03 and 4.29-5.96, respectively.

The linear partition coefficient (K_p) was calculated from Eq. (7). The result showed that the K_p values of DBAN adsorption on CF, CF-$FeCl_3$, and CF-$Fe(NO_3)_3$ were 0.77, 1.63, and 9.53 L/g, respectively. The highest K_p values of DBAN adsorption were found in CF-$Fe(NO_3)_3$ following CF-$FeCl_3$ and CF, respectively. It can be concluded that CF-$Fe(NO_3)_3$ has the highest efficiency to adsorb DBAN. When considering the pore structure of all adsorbents, CF-$Fe(NO_3)_3$ had a higher porosity than CF and CF-$FeCl_3$ [24]. Thus, it can be indicated that the pore structure of the adsorbent influenced the K_p value.

The Freundlich isotherm constant value was calculated from Eq. (8). The range of the 1⁄n value for all adsorbents was nearly 1. So, the Freundlich isotherm equation was transformed into a linear equation. Then, the K_F value was calculated as shown in Table 4. The results showed that the K_F values of DBAN adsorption on CF, CF-$FeCl_3$, and CF-$Fe(NO_3)_3$ were 0.49, 4.25, and 7.29 µg/g, respectively. It was the same trend with the linear isotherm, which can indicate that the CF-$Fe(NO_3)_3$ has the highest efficiency to adsorb DBAN.

The R-P isotherm constant value was calculated from Eq. (9). The value of β_R was equal to 0 (0.00018 L/µg) for all adsorbents. So, the R-P isotherm equation was transformed into a linear equation. Then, the K_R value was calculated as shown in Table 4. The results showed that the K_R values of DBAN adsorption on CF, CF-$FeCl_3$, and CF-$Fe(NO_3)_3$ were 0.76, 1.63, and 9.54 L/g, respectively. It was the same trend with the linear isotherm and the Freundlich isotherm which can be indicated that the CF-$Fe(NO_3)_3$ had the highest efficiency to adsorb DBAN.

From the obtained results of the three isotherm models, it can be concluded that CF-$Fe(NO_3)_3$ had a higher efficiency to remove DBAN than other adsorbents. Thus, it can be indicated that the activation of adsorbent with ferric nitrate can increase the efficiency of removing DBAN due to the increased of porosity of the adsorbent.

The D-R isotherm model was used to explain the type of adsorption mechanism by investigating the mean free adsorption energy (E). The mean free adsorption energy was defined as the change of free energy for transferring one mol of adsorbate to the surface of a solid [32]. The obtained E values from the DBAN adsorption on all adsorbents ranged from 0.04 to 0.37 kJ/mol. The E values that were lower than 8 indicate that the adsorption mechanism was mainly physical absorption [33]. So, it can be indicated that physical adsorption occurred for DBAN adsorption on all adsorbents, which is consistent with the adsorption kinetics results.

Adsorption kinetic of five HANs species removal using CF-Fe(NO_3)$_3$ adsorbent.

As shown in Figure 5, all the isotherm data shows a linear function. TCAN species was highly adsorbed by CF-$Fe(NO_3)_3$ and followed by DBAN, BCAN, DCAN, and MBAN, respectively. When considering the solubility of each HANs species, it was found that the adsorption capacity of CF-$Fe(NO_3)_3$ was inversely proportional to the solubility of the five HANs species.

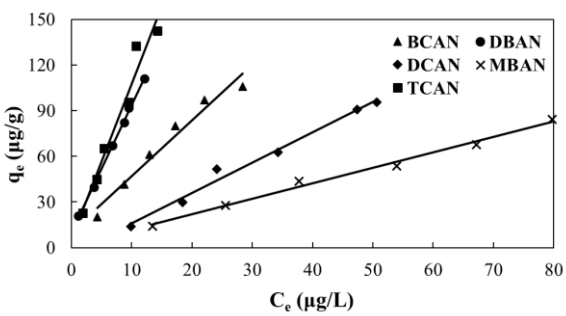

Figure 5 Adsorption isotherm of five HANs on CF-$Fe(NO_3)_3$

Table 5 shows the calculated isotherm parameters for five HANs adsorption on CF-Fe$(NO_3)_3$. The correlation coefficient (RRSME) from low to high was followed by linear ≈ Redlich-Peterson > Freundlich> Dubinin-Radushkevich, respectively. From the obtained results, it was found that the linear models were matched for the adsorption of all the HANs on CF-Fe$(NO_3)_3$ with a low RRSME in the range of 2.18-9.20.

The adsorption of five HANs species was fitted with linear isotherm, Freundlich isotherm, and R-P isotherm. The coefficient of each isotherm was calculated, including K_P, K_F, and K_R, respectively. All the calculated coefficients of each isotherm model showed the same trends for five HANs species. TCAN was found to have the highest coefficient values at 10.75 L/g, 13.59 μg/g, and 10.76 L/g for K_P, K_F, and K_R, respectively. It can be indicated that TCAN was easier to adsorb on the CF-Fe$(NO_3)_3$ than other species due to its characteristics, which have more hydrophobicity than other species. On the other hand, the lowest coefficient values were found for MBAN species at 1.04 L/g, 1.22 μg/g, and 1.04 L/g for K_P, K_F, and K_R, respectively. These results correspond with the characteristics of MBAN, which has the lowest hydrophobicity among all species.

In the D-R isotherm model, the E values for the adsorption of the five HANs species on the CF-Fe$(NO_3)_3$ ranged from 0.06 to 0.37 kJ/mol. Thus, it can be indicated that physical adsorption occurred for all five HANs species adsorption on CF-Fe$(NO_3)_3$. Low adsorption energy for all HANs species could be explained that all HANs species are more easily adsorbed onto the CF-Fe$(NO_3)_3$ adsorbents.

The effect of halogen atoms (Cl and Br) on HANs adsorption isotherm was also evaluated by comparing the adsorption isotherm of five HANs onto CF-Fe$(NO_3)_3$. The results showed the affinity of each HANs on the adsorbent from high to low were following TCAN > DBAN > BCAN > DCAN > MBAN, respectively with the same trends with the K_P value of each HANs species as shown in Table 5. When considering the halogen atoms of each HANs species, it was observed that HANs with a higher number of halogen atoms have higher K_P values where tri-HAN > di-HAN > mono-HAN. In addition, the Br-HAN was provided with a higher K_P than the Cl-HAN. The HANs species with a higher K_P value had a higher adsorption capacity. A high K_P value implies that the adsorbent has a high affinity for HAN adsorption [14].

Table 4 Isotherm parameters of DBAN adsorption on CF, CF-$FeCl_3$, and CF-Fe$(NO_3)_3$

Materials	**Linear isotherm**			**Redlich-Peterson isotherm**			
	K_p (L/g)	RRSME		K_R (L/g)	B (L/μg)	β_R	RRSME
CF	0.77	6.03		0.76	0.000	0.00000	5.96
CF-$FeCl_3$	1.63	4.41		1.63	0.001	0.00018	4.29
CF-Fe$(NO_3)_3$	9.53	4.78		9.54	0.001	0.00018	4.68
Materials	**Freundlich isotherm**			**Dubinin–Radushkevich isotherm**			
	K_F (μg/g)	$1/n$	RRSME	q_{DR} (μg/g)	B (mol^2/KJ^2)	E (KJ/mol)	RRSME
CF	0.49	0.72	27.88	90	35.6×10^{-11}	0.04	8.05
CF-$FeCl_3$	4.25	0.73	1.90	63	2.3×10^{-11}	0.15	6.62
CF-Fe$(NO_3)_3$	7.29	1.12	6.85	116	0.4×10^{-11}	0.37	10.82

Table 5 Isotherm parameters of DBAN adsorption on CF, CF-$FeCl_3$, and CF-$Fe(NO_3)_3$

HANs	Linear isotherm		Redlich-Peterson isotherm			
	K_p (L/g)	RRSME	K_R (L/g)	B (L/μg)	β_R	RRSME
BCAN	4.19	7.32	4.19	0.001	0.00018	7.26
DBAN	9.53	4.78	9.54	0.001	0.00018	4.68
DCAN	1.89	3.77	1.89	0.001	0.00018	3.64
MBAN	1.04	2.18	1.04	0.001	0.00018	1.93
TCAN	10.75	9.20	10.76	0.001	0.00018	9.15

HANs	Freundlich isotherm			Dubinin–Radushkevich isotherm			
	K_F (μg/g)	$1/n$	RRSME	q_{DR} (μg/g)	B (mol^2/KJ^2)	E (KJ/mol)	RRSME
BCAN	2.43	1.35	5.32	113	1.5×10^{-11}	0.18	8.32
DBAN	7.29	1.12	6.85	116	0.4×10^{-11}	0.37	10.82
DCAN	1.53	1.06	3.43	109	7.8×10^{-11}	0.08	7.09
MBAN	1.22	0.96	1.80	84	14.1×10^{-11}	0.06	8.06
TCAN	13.59	0.90	8.46	148	0.4×10^{-11}	0.34	13.45

Conclusion

The adsorption mechanism of HANs by canvas fabric adsorbents was investigated. Three different adsorbents were used in this study including the canvas fabric derived adsorbent (CF), activated canvas fabric derived adsorbent with $FeCl_3$ (CF-$FeCl_3$), and activated canvas fabric derived adsorbent with $Fe(NO_3)_3$ (CF-$Fe(NO_3)_3$). The activated adsorbent with $Fe(NO_3)_3$ increases the removal efficiency when considering adsorption kinetics and isotherms. The CF-$Fe(NO_3)_3$ adsorbent showed a mesopore structure with a larger porosity and the adsorption occurs not only outer the pore layer but also inside the pore surface. The larger pore volume of CF-$Fe(NO_3)_3$ resulted in a faster initial adsorption rate and half-life time of DBAN. In addition, the results of intraparticle diffusion showed that CF-$Fe(NO_3)_3$ was faster to adsorb DBAN than other adsorbents. When considering the adsorption kinetics of five HANs species, TCAN species showed the fastest rate to reach equilibrium within 30 minutes due to the lower solubility of TCAN. Thus, TCAN was highest adsorbed on CF-$Fe(NO_3)_3$ followed by MBAN, DCAN, BCAN, and DBAN, respectively. From the RRSME value of each kinetics model, it can indicate that the adsorption kinetics of five HANs species were fitted with a linear driving force model. Based on the D-R isotherm model, the adsorption mechanism of DBAN on all adsorbents was physical adsorption due to the lower E values. The results of linear, Freundlich, and R-P isotherm indicated that CF-$Fe(NO_3)_3$ had the highest efficiency in removing DBAN than other adsorbents. The results of the adsorption isotherm of five HANs species showed that TCAN was easier to adsorb on the CF-$Fe(NO_3)_3$ than other species due to its lower solubility. On the other hand, MBAN which had higher solubility had lower efficiency to adsorb on CF-$Fe(NO_3)_3$ adsorbent. In addition, TCAN with more halogen atoms (tri-HANs) resulted in a highly adsorbed on adsorbent. All HANs species were adsorbed on CF-$Fe(NO_3)_3$ adsorbent with a physical adsorption mechanism due to the low adsorption energy obtained from the D-R isotherm. The potential of reusing spent adsorbent through an efficient regeneration process will be further investigated based on the obtained results of the adsorbent mechanism. The kinetics and isotherm adsorption mechanisms of canvas fabric derived adsorbent and activated adsorbent with ferric solution were elucidated in this study. The next step of the research will focus on the potential of reusing spent adsorbent through an efficient regeneration process. The obtained results of the adsorbent mechanism revealed that physical adsorption occurred between HANs species and carbon material adsorbent, which were easier to remove from spent adsorbents. Then, the possible techniques for the regeneration process will be further investigated.

Acknowledgement

This research work was partially supported by the Graduate School of Chiang Mai University.

References

[1] Dubey, S., Gusain, D., Sharma, Y. C. and Bux, F. 2020. Chapter 15 - The occurrence of various types of disinfectant by-products (trihalomethanes, haloacetic acids, haloacetonitrile) in drinking water. Disinfection By-products in Drinking Water. Butterworth-Heinemann. 371-391.

[2] Han, J., Zhang, X., Jiang, J. and Li, W. 2021. How Much of the Total Organic Halogen and Developmental Toxicity of Chlorinated Drinking Water Might Be Attributed to Aromatic Halogenated DBPs?. Environmental Science and Technology. 55(9): 5906-5916.

[3] Cheng, J. B., Zhao, H. B., Zhang, A. N., Wang, Y. Q. and Wang, Y. Z. 2022. Porous carbon/Fe composites from waste fabric for high-efficiency electromagnetic wave absorption. Journal of Materials Science & Technology. 126: 266-274.

[4] Richardson, S. D. 2011. Disinfection By-Products: Formation and Occurrence in Drinking Water. Encyclopedia of Environmental Health. 110-136.

[5] Krasner, S. W., Weinberg, H. S., Richardson, S. D., Pastor, S. J., Chin, R., Sclimenti, M. J., Onstad, G. D. and Thruston, A. D. 2006. The occurrence of a new generation of disinfection by-products. Environmental Science & Technology. 40: 7175-7185.

[6] WHO. 2017. Guidelines for drinking-water quality: fourth edition incorporating the first addendum.

[7] Allen, J. M., Plewa, M. J., Wagner, E.D., Wei, X., Bokenkamp, K., Hur, K., Jia, A., Liberatore, H. K., Lee, C. F. T., Shirkhani, R. And Krasner, S. W. 2022. Drivers of Disinfection Byproduct Cytotoxicity in U.S. Drinking Water: Should Other DBPs Be Considered for Regulation?. Environmental Science and Technology. 56(1): 392-402.

[8] Jayawardana, T.K., Hossain, M. F., Patel, D. and Kimura, S. Y. 2023. Haloacetonitrile stability in cell culture media used in vitro toxicological studies. Chemosphere. 313: 137568.

[9] Ma, X., Cheng, J., Zhang, P., Wu, Y., Deng, J., Dong, F., Li, X. and Dietrich, A. M. 2024. Impact of boiling on chemical and physical processes for reduction of halomethanes, haloacetonitriles, and haloacetic acids in drinking water. Science of The Total Environment. 906: 167657.

[10] Shi, W., Wang, L. and Chen, B. 2017. Kinetics, mechanisms, and influencing factors on the treatment of haloacetonitriles (HANs) in water by two household heating devices. Chemosphere. 172: 278-285.

[11] Chang, X., Yao, X., Ding, N., Yin, X., Zheng, Q., Lu, S., Shuai, D. and Sun, Y. 2019. Photocatalytic degradation of trihalomethanes and haloacetonitriles on graphitic carbon nitride under visible light irradiation. Science of The Total Environment. 682: 200-207.

[12] Zhang, X., Yao, J., Zhao, Z. and Liu, J. 2019. Degradation of haloacetonitriles with UV/peroxymonosulfate process: Degradation pathway and the role of hydroxyl radicals. Chemical Engineering Journal. 364: 1-10.

[13] Zhang, D., Dong, S., Zhang, A., Chen, L., Yu, Z., Wang, Q. and Chu, W. 2021. Catalytic hydrolysis: A novel role of zero-valent iron in haloacetonitrile degradation and transformation in unbuffered systems. Science of The Total Environment. 801: 149537.

[14] Prarat, P., Ngamcharussrivichai, C., Khaodhiar, S. and Punyapalakul, P. 2019. Adsorption of single and mixed haloacetonitriles on silica-based porous materials: Mechanisms and effects of porous structures. Journal of Environmental Sciences. 79: 346-360.

[15] Prarat, P., Ngamcharussrivichai, C., Khaodhiar, S. and Punyapalakul, P. 2013. Removal of haloacetonitriles in aqueous solution through adsolubilization process by polymerizable surfactant-modified mesoporous silica. Journal of Hazardous Materials. 244-245: 151-159.

[16] Din, M. I., Ashraf, S. and Intisar, A. 2017. Comparative Study of Different Activation Treatments for the Preparation of Activated Carbon: A Mini-Review. Science Progress. 100(3): 299-312.

[17] Qian, H., Lin, Y. L., Xu, B., Wang, L. P., Gao, Z. C. and Gao, N. Y. 2018. Adsorption of haloforms onto GACs: Effects of adsorbent properties and adsorption mechanisms. Chemical Engineering Journal. 349: 849-859.

[18] Nakamura, T., Kawasaki, N., Araki, M., Yoshimura, K. and Tanada, S. Part A, 2001. TRIHALOMETHANE REMOVAL BY ACTIVATED CARBON FIBER. Journal of Environmental Science and Health. 36(7): 1303-1310.

[19] Numee, P., Sangtawesin, T., Yilmaz, M. and Kanjana, K. 2024. Activated carbon derived from radiation-processed durian shell for energy storage application. Carbon Resources Conversion. 7(2): 100192.

[20] Kuok, K. K., Chiu, P. C., Rahman, M. R., Chin, M. Y. and Bin Bakri, M. K. 2024. Sustainable bamboo and coconut shell activated carbon for purifying river water on Borneo Island. Waste Management Bulletin. 2(1): 39-48.

[21] Xu, Z., Tian, D., Sun, Z., Zhang. D/. Zhou, Y., Chen, W. And Deng, H. 2019. Highly porous activated carbon synthesized by pyrolysis of polyester fabric wastes with different iron salts: Pore development and adsorption behavior. Colloids and Surfaces A: Physicochemical and Engineering Aspects. 565: 180-187.

[22] Dridi-Dhaouadi, S., Douissa-Lazreg, B. N. and M'Henni, M. F. 2011. Removal of lead and yellow 44 acid dye in single and binary component systems by raw Posidonia oceanica and the cellulose extracted from the raw biomass. Environmental technology. 32(3-2): 325-340.

[23] Sandin, G. and Peters, G.M. 2018. Environmental impact of textile reuse and recycling - A review. Journal of Cleaner Production. 184: 353-365.

[24] Yimyam, K., Wongrueng, A. and Rakruam, P. 2023. Haloacetonitriles adsorption using a low-cost adsorbent derived from canvas fabric. Environmental Research. 234: 116539.

[25] Ho, Y. S. and McKay, G. 1998. Sorption of dye from aqueous solution by peat. Chemical Engineering Journal. 70(2): 115-124.

[26] Weber Jr, W. and Morris, J. 1963. Kinetics of Adsorption on Carbon from Solution. Journal of Scientific and Engineering Division.

[27] Rodrigues, A. E. and Silva, C. M. 2016. What's wrong with Lager green pseudo first order model for adsorption kinetics?. Chemical Engineering Journal. 306: 1138-1142.

[28] Wu, F. C., Tseng, R. L., Huang, S. C. and Juang, R. S. 2009. Characteristics of pseudo-second-order kinetic model for liquid-phase adsorption: A mini-review. Chemical Engineering Journal. 151(1): 1-9.

[29] Ruiz, B., Cabrita, I., Mestre, A. S., Parra, J. B., Pires, J., Carvalho, A. P. and Ania, C. O. 2010. Surface heterogeneity effects of activated carbons on the kinetics of paracetamol removal from aqueous solution. Applied Surface Science. 256(17): 5171-5175.

[30] Liu, Q. S., Zheng, T., Wang, P., Jiang, J. P. and Li, N. 2010. Adsorption isotherm, kinetic and mechanism studies of some substituted phenols on activated carbon fibers. Chemical Engineering Journal. 157(2): 348-356.

[31] Ozcan, A., Ozcan, A. and Gok, O. 2007. Adsorption kinetics and isotherms of anionic dye of reactive blue 19 from aqueous solutions onto DTMA-sepiolite. Hazardous Materials and Wastewater-Treatment, Removal and Analysis. Nova Science Publishers. New York.

[32] Zhan, Y., Lin, J. and Zhu, Z. 2011. Removal of nitrate from aqueous solution using cetylpyridinium bromide (CPB) modified zeolite as adsorbent. Journal of Hazardous Materials. 186(2): 1972-1978.

[33] Abin-Bazaine, A., Trujillo, A. C. and Olmos-Marquez, M. 2022. Adsorption Isotherms: Enlightenment of the Phenomenon of Adsorption. Wastewater Treatment. Intechopen: 104260.